Research in Astronomy and Astrophysics, 22:075001 (13pp), 2022 July https://doi.org/10.1088/1674-4527/ac684e

Multicolor Optical Monitoring of the γ -Ray Emitting Narrow-line Seyfert 1 Galaxy PMN J0948+0022 from 2020 to 2021

Yu-Xin Xin[1,2,3,4], Ding-Rong Xiong[1,3,4], Jin-Ming Bai[1,3,4], Hong-Tao Liu[1,3,4], Kai-Xing Lu[1,3,4], and Ji-Rong Mao[1,3,4]
[1] Yunnan Observatories, Chinese Academy of Sciences, Kunming 650216, China; xiongdingrong@ynao.ac.cn, baijinming@ynao.ac.cn
[2] University of Chinese Academy of Sciences, Beijing 100049, China
[3] Key Laboratory for the Structure and Evolution of Celestial Objects, Chinese Academy of Sciences, Kunming 650216, China
[4] Center for Astronomical Mega-Science, Chinese Academy of Sciences, Beijing 100101, China
Received 2022 February 28; revised 2022 April 1; accepted 2022 April 18; published 2022 June 14

Abstract

In order to study the physical properties of the γ-ray emitting narrow-line Seyfert 1 (NLS1) galaxy population, photometric and spectral observations of the γ-ray emitting NLS1 PMN J0948+0022 were made with the Lijiang 2.4 m optical telescope of Yunnan Observatories, Chinese Academy of Sciences. Photometric data in the *B* and *R* bands were collected for 50 nights from 2020 January to 2021 December. During the observation epoch, the variability amplitudes are 73.67% in the *B* band and 79.96% in the *R* band. Intra-day variability is found in two observation nights, and the duty cycle value is 29% with variability amplitude > 12.9% in the *R* band, which support the presence of the relativistic jets in the target. The redder-when-brighter (RWB) chromatic trend (or steeper-when-brighter trend) appears on intra-day and long timescales. The RWB trend is dominated by the radiation of accretion disk and jet, and resembles those in flat spectrum radio quasars. When PMN J0948+0022 is brighter than $17^{\mathrm{m}}.5$ in the *R* band, there is no color change trend. By analyzing the spectral data of PMN J0948+0022, we obtained the black hole mass of $M_{\bullet} = 1.61 \times 10^7 M_{\odot}$ and accretion rate of $\dot{\mathscr{M}} = 93$, and confirmed that PMN J0948+0022 is a super-Eddington accreting NLS1. The redshifts of reverberation mapped super-Eddington accreting active galactic nuclei can be expanded by PMN J0948+0022 up to above 0.5. Super-Eddington accreting NLS1 galaxies were chosen as a new type of cosmological candle in the literature. PMN J0948+0022 may be used as a target for the next step of reverberation mapping monitoring project of super-Eddington accreting massive black holes.

Key words: galaxies: jets – galaxies: photometry – galaxies: Seyfert – galaxies: active

1. Introduction

Active galactic nuclei (AGNs) are very energetic phenomena in the central regions of galaxies and are powered by accretion processes of black holes other than the nuclear fusion that powers stars (Urry & Padovani 1995). Seyfert galaxy is a subclass of AGNs. Osterbrock & Pogge (1985) first proposed the concept of narrow-line Seyfert 1 (NLS1) galaxies when they classified the Seyfert galaxies. Compared to normal Seyfert 1 galaxies, the optical spectra of NLS1 galaxies contain narrower permitted broad emission lines from broad-line region (BLR), with full width at half maximum (FWHM) < 2000 km s^{-1} for broad emission line Hβ (Goodrich 1989; Pogge 2000). Besides, they have a line ratio [O III]/Hβ < 3, strong permitted Fe II emission lines, a steep soft X-ray spectrum, and rapid variabilities in the optical and X-ray bands (Shuder & Osterbrock 1981; Boller et al. 1996; Yuan et al. 2008; Liu et al. 2010; Paliya et al. 2013; Berton et al. 2015; Kshama et al. 2017; Wang et al. 2017; D'Ammando 2020; Ojha et al. 2020, 2021). Though controversial, it is widely believed that the centers of NLS1 galaxies possess black holes with relatively small masses and high accretion rates (Williams et al. 2002; Zhou et al. 2003; Yuan et al. 2008; Abdo et al. 2009a; Calderone et al. 2013; Berton et al. 2015; Baldi et al. 2016; Ojha et al. 2020). According to radio-loudness parameter *R*, NLS1 galaxies are divided into two categories: radio-loud (*R* > 10) and radio-quiet (*R* < 10). Most of them belong to radio-quiet NLS1 galaxies (93%) while the fraction of radio-loud NLS1 galaxies is only 7% (Komossa et al. 2006; Zhou et al. 2006; Kellermann et al. 2016). For the extremely radio-loud NLS1 galaxies (*R* > 100), the fraction falls to 2%–3% (Komossa et al. 2006; Yuan et al. 2008).

Similar to blazars, a few radio-loud NLS1 galaxies show high radio brightness temperatures, flat radio spectrum, and optical intra-day variability (IDV) (Zhou et al. 2003; Yuan et al. 2008; Liu et al. 2010; Gu et al. 2015). These characteristics support that at least these radio-loud NLS1 galaxies carry relativistic jets. Owing to high sensitivity, Fermi Large Area Telescope (LAT) has detected high-energy γ-ray emission (*E* > 100 MeV) from radio-loud NLS1 galaxies, definitely confirming relativistic jets in these radio-loud NLS1 galaxies (Abdo et al. 2009a, 2009b, 2009c; Foschini et al. 2011). In addition to blazars and radio galaxies, radio-loud Seyfert 1 galaxies also join the catalog of γ-ray AGNs. About 15 NLS1 galaxies have been detected in the γ-ray band (Yao et al. 2019), nine of which are contained in the fourth catalog of AGNs from the Fermi LAT (4LAC) (Ajello et al. 2020). The detections of γ-ray emitting NLS1 galaxies open new and interesting questions on the unified model of AGNs, development of relativistic jets, and evolution of radio-loud AGNs (Yuan et al. 2008; Abdo et al. 2009b). Finding evidence of blazar-like behavior in γ-ray emitting NLS1 galaxies would help to understand the evolution of relativistic jets (Itoh et al. 2013) and to answer whether γ-ray emitting NLS1 galaxies are a new blazar population (Eggen et al. 2013).

Based on the fact that the bolometric luminosities of AGNs tend to saturate at super-Eddington accretion rates, Wang et al. (2013) suggest that super-Eddington AGNs can be used as a new type of cosmological candle. In order to test this suggestion, a large reverberation mapping monitoring project is developed by group of Super-Eddington Accreting Massive Black Holes (SEAMBHs) to measure the masses and accretion rates of supermassive black holes (SMBHs) (Du et al. 2014; Hu et al. 2015). An interesting fact is that almost all the NLS1 galaxies selected as the SEAMBH candidates are confirmed to be super-Eddington accreting AGNs, but they are radio-quiet and no γ-ray emitting. The radio-loud and γ-ray emitting NLS1 galaxies are the potential candidates of super-Eddington accreting AGNs, and their physical properties and their connections with the normal AGNs are not yet fully understood. Therefore, it is quite interesting to perform observation of the γ-ray emitting NLS1 galaxies.

PMN J0948+0022 (R.A. = 09:48:57.32, decl. = +00:22:25.56, J2000, $z = 0.5846$) is the first radio-loud NLS1 galaxy ($R > 1000$) detected in γ-rays (Abdo et al. 2009a, 2009b), and is considered as the prototype for γ-ray emitting NLS1 galaxies. Abdo et al. (2009a) discovered that the NLS1 galaxy strongly displays variable emission in the radio and γ-ray bands, high brightness temperatures, variability of the compact radio core, and a flat and inverted radio spectrum. Liu et al. (2010) first found the optical IDV in the NLS1 galaxy. The high polarization degree in the optical band was also reported (e.g., Ikejiri et al. 2011; Eggen et al. 2013; Itoh et al. 2013). The above results indicate the presence of a relativistic jet for the γ-ray emitting NLS1 galaxy. Although PMN J0948+0022 is a good target to study the properties of new γ-ray emitting NLS1 galaxy population and to find similarities to blazars, its optical flux variability on different timescales is still not fully studied. Optical flux variability is often associated with color/spectral behavior in blazars, which can be used to explore the radiation mechanism and origin of flux variability (Wu et al. 2007; Gu 2011; Dai et al. 2015; Xiong et al. 2016, 2017; Feng et al. 2020a, 2020b). For γ-ray emitting NLS1 galaxies, the relationships between optical flux and color have been hardly explored.

In view of these facts and in order to analyze flux variability and spectral properties, we carried out multicolor optical monitoring and spectroscopic observations of the target from 2020 to 2022 using the Lijiang 2.4 m optical telescope. This paper is organized as follows. We describe photometric and spectroscopic observations and data reduction in Section 2. The results are given in Section 3. Discussion and conclusions are presented in Sections 4 and 5, respectively.

2. Observations and Data Reduction

2.1. Photometry

The long-term optical monitoring program of γ-ray emitting NLS1 galaxy PMN J0948+0022 was carried out using the Lijiang 2.4 m telescope with the primary scientific instrument-Yunnan Faint Object Spectrograph and Camera (YFOSC, Fan et al. 2015; Wang et al. 2019). The instrument is mounted on the straight Cassegrain focal plane of the Lijiang 2.4 m telescope, covers the wavelength range from 350 nm to 1100 nm, and has an image scale of $0\farcs283$ pixel^{-1} in the standard readout mode and a field of view (FoV) of 10×10 arcmin^2. The detector is CCD42-90 back illuminated deep depletion 2048×4612 pixel E2V Scientific CCD Sensor, with pixel size 13.5×13.5 μm^2. The full frame was for spectroscopic observation and the half frame of 2148x2200 was for photometric observation.

Our photometry observations were performed in a cyclic mode among the standard Johnson B and R bands. Before 2020 December 19, the exposure times were 300 s and 150 s for the B and R bands, respectively, under CCD readout mode of bin2. Afterwards, the exposure times were 600 s and 300 s for the B and R bands, respectively, under CCD readout mode of bin1. The bin2 mode combined 2×2 pixels into 1 pixel and its readout noise is 2.8 e^-. The bin1 mode had not merged pixels and its readout noise is 6.3 e^-. Both of them have the same gain 0.3 e^- ADU^{-1}. The time resolutions per night for the same bands were from 8 to 16.5 minutes. The time interval between the B and R bands in the same cycle was less than 15 minutes. So, the B band and R band observations could be considered as quasi-simultaneous measurements.

The photometric data processing program is implemented based on Python3, which mainly includes astronomy package —Astropy (Thomas et al. 2013; Price-Whelan 2018), astrometry software—Astrometry.Net and photometric software—SExtractor.[5] The details are described below.

(i) Data classification: All photometric observations on YFOSC were automatically classified into three groups: bias, flat and science data. Based on the bias and flat data, we could get the gain and readout noise values (Howell 2006). Flat field

[5] https://sextractor.readthedocs.io/en/latest/

images were observed during the twilight when clear. If there were no flat field images on that night, the flat field images on the latest date was selected. The bias images were observed at the beginning and end of the observations. We need to check every fits image before using it.

(ii) Pre-processing: We stacked 10 bias images and calculated the median value as the masterbias. For flat field image, first we trimmed the flat image data as the same size of the trimmed object image; second we used the median of the image data as the divisor to achieve flat field normalization; finally use the median of the normalized flat field as the masterflat. During the data pre-processing, the science data were trimmed (remove invalid areas around the FoV) and corrected by masterbias and masterflat. Furthermore, the cosmic ray elimination program would be performed when the cosmic ray contaminated the target or the reference stars, and this program has the same function as IRAF by using the Laplacian Cosmic Ray Identification[6] (Pieter & van 2001). We used Astrometry.net to get new world coordinate system coordinates and updated them in fits header. The higher photometric coordinates could be obtained by SExtractor (Bertin & Arnouts 1996).

(iii) Aperture photometry: We extracted instrument magnitudes of all the objects using the SOURCE-EXTRACTOR (SExtractor2.19.5, Kron 1980). SExtractor's automatic aperture photometry routine was derived from Kron's "first moment" algorithm (Kshama et al. 2017). Since there are no nearby stars around the target and comparison stars, we utilized MAG_AUTO to get the best magnitudes. The MAG_AUTO could automatically select the best aperture to measure the instrument magnitudes in each measurement. The aperture radii ranged from 2 × FWHM to 5 × FWHM and the average value is 3.8 × FWHM, where FWHM denotes seeing. We checked the aperture radius of 5 × FWHM, but could not find any stars other than the target within the aperture.

(iv) Differential photometry and errors: We obtained the source magnitude from the average of the values derived with respect to two comparison stars in the same frame (e.g., Zhang et al. 2008; Fan et al. 2014; Xiong et al. 2016, 2017). The finding chart of the target is presented in Figure 1. The Landessternwarte Königstuhl (LSW)[7] at the University of Heidelberg provided the chart for the same field. The LSW marks out three stars (A, B and C) as comparison stars. A and B comparison stars were chosen because their magnitudes are known and their locations are close to the target. Maune et al. (2013) confirmed that the two comparison stars were stable. The magnitudes of the two comparison stars were obtained from the LSW (A: $m_B = 17^{\rm m}\!.84$, $m_R = 16^{\rm m}\!.35$; B: $m_B = 17^{\rm m}\!.23$, $m_R = 16^{\rm m}\!.33$). In order to further illustrate that the two comparison stars are stable during our observation period, the differential instrumental magnitudes between them are shown in Figure 2. As shown in Figure 2, the comparison stars are stable. The standard deviations of differential instrumental magnitudes between them are 0.017 in the *R*-band and 0.048 in the *B*-band. Although a few values in the *B*-band have large deviations from average value of differential magnitudes between A and B stars, the rms errors of the differential magnitudes can reflect these deviations. The rms errors of the differential magnitudes between two comparison stars on a certain night were regarded as photometry errors (see Zhang et al. 2008; Fan et al. 2014; Xiong et al. 2016, 2017). The photometric data are given in Table 1. For a few nights, insufficient sampling (once or twice a night) caused that there was no rms errors or the errors were zero. We used the average error in each band as the error of the night observed only once, and the minimum error instead of the zero error.

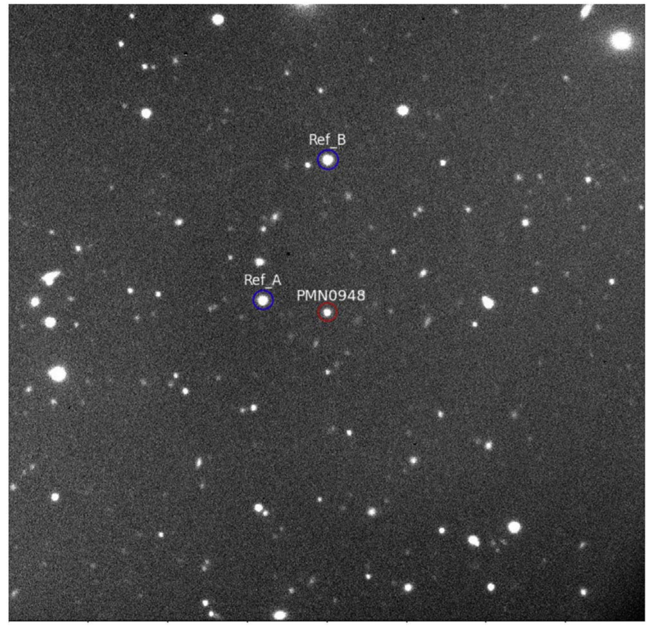

Figure 1. The finding chart of of PMN J0948+0022. The red circle is the target and the blue circles are two comparison stars (FoV is $7\!'.6 \times 7\!'.6$).

2.2. Spectroscopy

Using the Lijiang 2.4-m telescope, we obtained an optical spectrum of PMN J0948+0022 on 2022 February 11, which is near to the photometric period. The optical spectrum can be used to estimate the mass and accretion rate of the supermassive black hole in PMN J0948+0022. During the spectroscopic observation, we oriented the long slit to take the spectra of PMN J0948+0022 and a nearby comparison star simultaneously, and this method was widely used by many spectroscopic monitoring campaigns for spectral calibration (e.g.,

[6] http://www.astro.yale.edu/dokkum/lacosmic/

[7] https://www.lsw.uni-heidelberg.de/projects/extragalactic/charts/0948+002.html

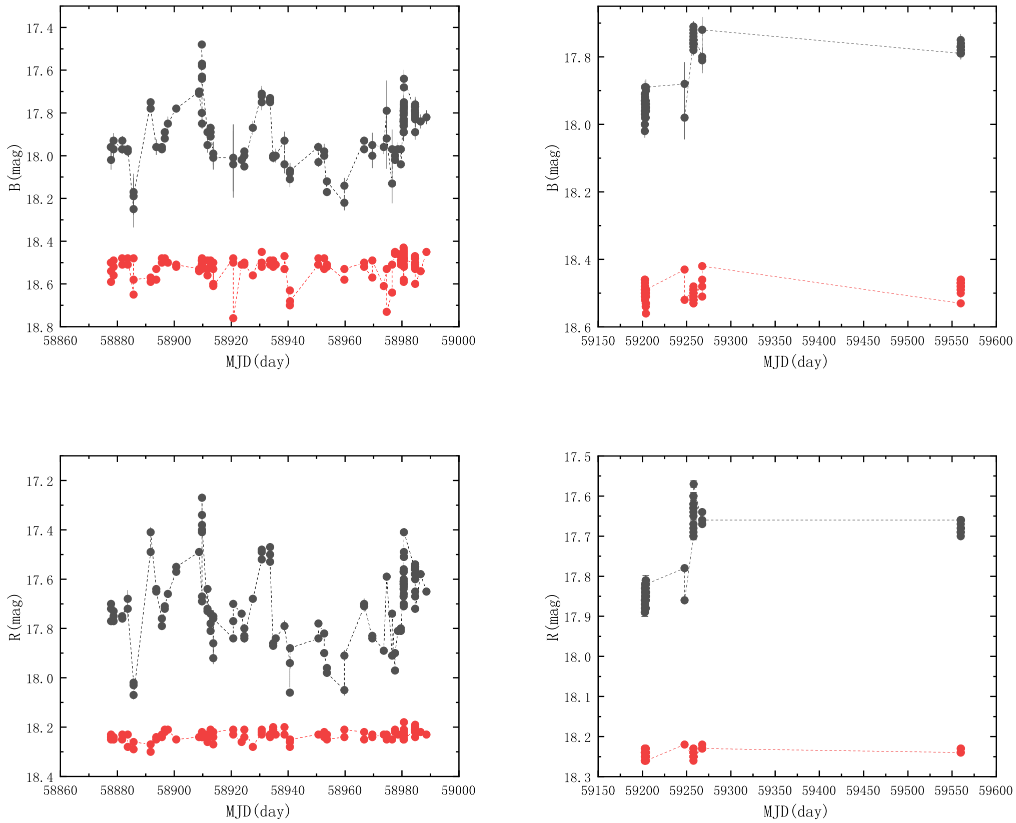

Figure 2. The long-term light curves of PMN J0948+0022 in different bands. The black circles represent the light curves of PMN J0948+0022. The red circles are the differential instrumental magnitudes between two comparison stars. The differential instrumental magnitudes are offset to avoid their eclipsing with the light curves of PMN J0948+0022.

Du et al. 2015; Lu et al. 2021a). Meanwhile, a standard star with a similar airmass to PMN J0948+0022 was selected. The two-dimensional spectroscopic image of PMN J0948+0022 was reduced using the standard IRAF procedures. We extracted the spectrum using the aperture of 20 pixels ($5''.7$), and background was determined from two adjacent regions ($+7''.4 \sim +14''$ and $-7''.4 \sim -14''$) on both sides of the aperture region. The red side of optical spectrum is contaminated by the variable absorptions of the telluric atmosphere, as a part of broad Hβ line drops into the absorption band of Oxygen in the observed frame. We used the correction method of the telluric absorption presented in Lu et al. (2021b) to correct the telluric absorption lines. In briefly, the spectra of PMN J0948+0022 and the comparison star have the same telluric transmission spectrum. The telluric spectrum can be constructed by dividing the observed spectrum of the comparison star with its stellar template. It was used to correct the telluric absorption lines in the observed spectrum of PMN J0948+0022. Then we calibrated the spectral flux of PMN J0948+0022 using the spectrum of standard star, and corrected the Galactic extinction using the extinction map of Schlegel et al. (1998) and the redshift. Meanwhile, we also took the photometric observations for PMN J0948+0022 at the night, 25 minutes before the Spectroscopic observations. The result shows that $B = 17^{\mathrm{m}}.85$ and $R = 17^{\mathrm{m}}.74$ with corrected for Galactic extinction.

3. Results

3.1. Long-term Optical Variability

The B band and R band magnitudes are corrected for the Galactic extinction with $A_B = 0.285$ and $A_R = 0.17$ from the NASA/IPAC Extragalactic Database (NED) and Schlafly & Finkbeiner (2011). Throughout, the rest of the article, the B band and R band magnitudes refer to the magnitudes corrected for the Galactic extinction. Figure 2 shows the long-term light curves in different bands from 2020 January 29 to 2021 December 11. In order to better display the light curves, we divide the observation epoch into two parts, in which the first epoch is from 2020 January 29 to 2020 May 19 (the left panel in Figure 2) and the second epoch is from 2020 December 19 to 2021 December 11 (the right panel in Figure 2).

For long timescales, the object displays significant variability in the B and R bands. The variability amplitude (Amp) is calculated as (Heidt & Wagner 1996)

$$\mathrm{Amp} = 100 \times \sqrt{(A_{\max} - A_{\min})^2 - 2\sigma^2} \text{ percent}, \qquad (1)$$

Table 1
Raw Photometric Data of PMN0948

JB			JR			JB			JR		
MJD	Mag	Error	MJD	Mag	Error	MJD	Mag	Error	MJD	Mag	Error
58877.7597	18.25	0.045	58877.7632	17.87	0.010	58980.6014	18.12	0.041	58980.6049	17.79	0.016
58877.7681	18.30	0.045	58877.7715	17.95	0.010	58980.6069	18.17	0.041	58980.6104	17.80	0.016
58877.7736	18.25	0.045	58877.7778	17.89	0.010	58980.6153	18.13	0.041	58980.6194	17.77	0.016
58878.6986	18.25	0.035	58878.7021	17.94	0.006	58980.6215	18.06	0.041	58980.6250	17.74	0.016
58878.7042	18.26	0.035	58878.7076	17.90	0.006	58980.6271	18.09	0.041	58980.6306	17.80	0.016
58878.7097	18.21	0.035	58878.7139	17.92	0.006	58980.6326	18.06	0.041	58980.6361	17.73	0.016
58881.7132	18.26	0.021	58881.7167	17.93	0.014	58980.6382	18.05	0.041	58980.6424	17.79	0.016
58881.7188	18.22	0.021	58881.7222	17.93	0.014	58980.6444	18.05	0.041	58980.6479	17.68	0.016
58883.6604	18.27	0.021	58883.6639	17.85	0.035	58980.6500	18.04	0.041	58980.6535	17.66	0.016
58883.666	18.25	0.021	58883.6694	17.89	0.035	58980.6556	17.97	0.041	58980.6590	17.68	0.016
58885.6806	18.53	0.085	58885.6847	18.19	0.017	58980.6611	17.93	0.041	58980.6653	17.59	0.016
58885.6861	18.45	0.085	58885.6903	18.20	0.017	58984.5840	18.08	0.035	58984.5882	17.73	0.013
58885.6924	18.47	0.085	58885.6965	18.24	0.017	58984.5903	18.06	0.035	58984.5938	17.75	0.013
58891.6833	18.03	0.014	58891.6875	17.66	0.021	58984.5958	18.08	0.035	58984.5993	17.71	0.013
58891.6896	18.06	0.014	58891.6931	17.58	0.021	58984.6014	18.05	0.035	58984.6049	17.73	0.013
58893.6597	18.25	0.035	58893.6653	17.81	0.007	58984.6069	18.10	0.035	58984.6111	17.77	0.013
58893.6674	18.25	0.035	58893.6729	17.82	0.007	58984.6132	18.05	0.035	58984.6167	17.73	0.013
58895.6639	18.24	0.014	58895.6694	17.93	0.007	58984.6188	18.10	0.035	58984.6222	17.72	0.013
58895.6715	18.26	0.014	58895.6771	17.96	0.007	58984.6243	18.06	0.035	58984.6278	17.75	0.013
58896.6937	18.20	0.007	58896.6972	17.89	0.007	58984.6299	18.09	0.035	58984.6340	17.82	0.013
58896.7000	18.18	0.007	58896.7035	17.88	0.007	58984.6361	18.18	0.035	58984.6396	17.84	0.013
58897.7618	18.13	0.032[a]	58897.7653	17.84	0.013	58984.6417	18.11	0.035	58984.6451	17.89	0.013
58900.6931	18.07	0.007	58900.6965	17.75	0.006[b]	58986.5444	18.12	0.032	58986.5479	17.75	0.013[b]
58900.6986	18.06	0.007	58900.7063	17.72	0.006[b]	58988.5660	18.11	0.032	58988.5639	17.82	0.013[b]
58908.7278	17.98	0.007	58908.7319	17.66	0.006[b]	59202.7290	18.30	0.019	59202.7357	18.04	0.010
58908.7340	18.00	0.007	58908.7375	17.66	0.006[b]	59202.7400	18.22	0.019	59202.7477	18.06	0.010
58909.7167	18.08	0.023	58909.7208	17.84	0.006	59202.7519	18.28	0.019	59202.7597	18.06	0.010
58909.7229	18.13	0.023	58909.7271	17.84	0.006	59202.7646	18.23	0.019	59202.7723	18.05	0.010
58909.7312	18.13	0.023	58909.7292	17.86	0.006	59202.7767	18.23	0.019	59202.7848	18.06	0.010
58909.7146	17.77	0.014	58909.7181	17.44	0.007	59202.7896	18.22	0.019	59202.7972	18.04	0.010
58911.6778	18.18	0.035	58911.6813	17.89	0.015	59202.8761	18.25	0.019	59202.8844	18.05	0.010
58911.6833	18.23	0.035	58911.6875	17.81	0.015	59202.8885	18.23	0.019	59202.8962	18.01	0.010
58912.7389	18.16	0.015	58912.7431	17.98	0.006	59202.9009	18.20	0.019	59202.9093	18.04	0.010
58912.7444	18.20	0.015	58912.7486	17.95	0.006	59202.9141	18.23	0.019	59202.9218	18.02	0.010
58912.7507	18.17	0.015	58912.7542	17.91	0.006	59202.9262	18.27	0.019	59202.9348	18.05	0.010
58913.6979	18.27	0.054	58913.7035	17.92	0.024	59202.9396	18.20	0.019	59202.9480	18.05	0.010
58920.6889	18.30	0.156	58920.6924	18.02	0.012	59203.8198	18.24	0.023	59203.7966	18.04	0.012
58920.6944	18.30	0.156	58920.6979	17.94	0.012	59203.8319	18.23	0.023	59203.8035	18.05	0.012
58920.7000	18.32	0.156	58920.7035	17.87	0.012	59203.8436	18.27	0.023	59203.8152	18.01	0.012
58923.6222	18.30	0.032[a]	58923.6257	17.91	0.013[b]	59203.8553	18.24	0.023	59203.8276	18.03	0.012
58924.6139	18.29	0.006	58924.6181	18.00	0.017	59203.8671	18.23	0.023	59203.8395	18.05	0.012
58924.6194	18.27	0.006	58924.6236	17.97	0.017	59203.8788	18.22	0.023	59203.8512	18.02	0.012
58924.6257	18.34	0.006	58924.6292	18.02	0.017	59203.8905	18.19	0.023	59203.8629	18.02	0.012
58927.6236	18.16	0.032[a]	58927.6271	17.85	0.013[b]	59203.9025	18.23	0.023	59203.8747	18.01	0.012
58930.7063	17.99	0.036	58930.7097	17.69	0.010	59203.9144	18.23	0.023	59203.8864	18.02	0.012
58930.7132	18.04	0.036	58930.7174	17.66	0.010	59203.9262	18.23	0.023	59203.8984	18.01	0.012
58930.7194	18.01	0.036	58930.7229	17.65	0.010	59203.9379	18.24	0.023	59203.9101	17.98	0.012
58933.6410	18.01	0.012	58933.6444	17.64	0.006	59203.9496	18.18	0.023	59203.9220	17.99	0.012
58933.6465	18.02	0.012	58933.6500	17.67	0.006	59247.6758	18.16	0.064	59247.6832	17.95	0.006[b]
58933.6521	18.03	0.012	58933.6556	17.70	0.006	59247.6871	18.27	0.064	59247.6945	18.03	0.006[b]
58934.7222	18.30	0.021	58934.7264	18.04	0.007	59257.6430	18.03	0.015	59257.6504	17.88	0.009
58934.7285	18.28	0.021	58934.7319	18.04	0.007	59257.6544	18.04	0.015	59257.6618	17.86	0.009
58935.6694	18.28	0.032	58935.6729	18.01	0.013[b]	59257.6657	18.05	0.015	59257.6732	17.87	0.009
58938.6785	18.22	0.042	58938.6819	17.96	0.021	59257.6771	18.06	0.015	59257.6845	17.84	0.009
58938.6840	18.32	0.042	58938.6875	17.96	0.021	59257.6885	18.04	0.015	59257.6959	17.86	0.009
58940.6403	18.37	0.036	58940.6444	18.11	0.015	59257.6998	18.03	0.015	59257.7072	17.81	0.009
58940.6465	18.39	0.036	58940.6500	18.23	0.015	59257.7112	18.04	0.015	59257.7186	17.82	0.009

Table 1
(Continued)

JB			JR			JB			JR		
MJD	Mag	Error	MJD	Mag	Error	MJD	Mag	Error	MJD	Mag	Error
58940.6521	18.35	0.036	58940.6556	18.05	0.015	59257.7226	18.03	0.015	59257.7300	17.80	0.009
58950.6000	18.24	0.021	58950.6035	18.01	0.006[b]	59257.7339	18.05	0.015	59257.7413	17.82	0.009
58950.6056	18.32	0.021	58950.6097	17.95	0.006[b]	59257.7453	18.04	0.015	59257.7527	17.80	0.009
58952.6667	18.27	0.035	58952.6701	17.99	0.014	59257.7567	18.02	0.015	59257.7641	17.77	0.009
58952.6722	18.29	0.035	58952.6757	18.07	0.014	59257.7681	18.02	0.015	59257.7755	17.80	0.009
58953.6132	18.45	0.007	58953.6174	18.13	0.014	59257.7794	18.05	0.015	59257.7868	17.79	0.009
58953.6194	18.40	0.007	58953.6229	18.16	0.014	59257.7908	18.01	0.015	59257.7982	17.80	0.009
58959.7236	18.51	0.035	58959.7271	18.22	0.021	59257.8021	17.99	0.015	59257.8095	17.77	0.009
58959.7292	18.42	0.035	58959.7333	18.08	0.021	59257.8135	18.00	0.015	59257.8209	17.79	0.009
58966.6944	18.22	0.014	58966.6979	17.88	0.021	59257.8248	18.02	0.015	59257.8323	17.75	0.009
58966.7000	18.25	0.014	58966.7042	17.88	0.021	59267.6217	18.09	0.038	59267.6291	17.84	0.005
58969.5757	18.28	0.057	58969.5792	18.01	0.007	59267.6330	18.09	0.038	59267.6404	17.81	0.005
58969.5813	18.23	0.057	58969.5847	18.00	0.007	59267.6444	18.09	0.038	59267.6518	17.83	0.005
58973.5889	18.25	0.032[a]	58973.6007	18.07	0.013[b]	59267.6557	18.00	0.038	59267.6631	17.84	0.005
58974.5861	18.07	0.141	58974.5903	17.76	0.014	59541.8518	18.26	0.014	59541.8594	18.25	0.035
58974.5924	18.20	0.141	58974.5958	17.77	0.014	59541.8634	18.28	0.014	59541.8709	17.77	0.035
58976.5361	18.42	0.092	58976.5410	18.09	0.006[b]	59559.7425	18.08	0.017	59559.7499	17.83	0.005
58976.5431	18.26	0.092	58976.5479	17.91	0.006[b]	59559.7538	18.05	0.017	59559.7612	17.84	0.005
58977.5646	18.30	0.007	58977.5681	18.14	0.007	59559.7652	18.07	0.017	59559.7726	17.87	0.005
58977.5701	18.29	0.007	58977.5736	18.07	0.007	59559.7765	18.06	0.017	59559.7840	17.83	0.005
58978.5486	18.25	0.032[a]	58978.5521	17.98	0.013	59559.7879	18.04	0.017	59559.7953	17.83	0.005
58979.6000	18.26	0.014	58979.6035	17.98	0.006[b]	59559.7993	18.08	0.017	59559.8067	17.86	0.005
58979.6056	18.32	0.014	58979.6090	17.98	0.006[b]	59559.8107	18.06	0.017	59559.8181	17.84	0.005
58980.5437	18.09	0.041	58980.5472	17.78	0.016	59559.8220	18.07	0.017	59559.8295	17.84	0.005
58980.5493	18.13	0.041	58980.5535	17.74	0.016	59559.8334	18.08	0.017	59559.8408	17.86	0.005
58980.5556	18.08	0.041	58980.5590	17.79	0.016	59559.8448	18.07	0.017	59559.8522	17.86	0.005
58980.5611	18.11	0.041	58980.5646	17.79	0.016	59559.8562	18.05	0.017	59559.8636	17.86	0.005
58980.5667	18.12	0.041	58980.5701	17.81	0.016	59559.8675	18.07	0.017	59559.8750	17.85	0.005
58980.5722	18.14	0.041	58980.5764	17.84	0.016	59559.8789	18.05	0.017	59559.8864	17.84	0.005
58980.5785	18.18	0.041	58980.5819	17.88	0.016	59559.8903	18.04	0.017	59559.8977	17.85	0.005
58980.5840	18.17	0.041	58980.5875	17.87	0.016	59559.9017	18.06	0.017	59559.9091	17.84	0.005
58980.5896	18.14	0.041	58980.5931	17.83	0.016	59559.9131	18.05	0.017	59559.9205	17.84	0.005
58980.5951	18.12	0.041	58980.5993	17.80	0.016	…	…	…	…	…	

Notes.
[a] We used the average error in each band as the error of the night observed only once.
[b] We used minimum error instead of zero error.

where A_{min} and A_{max} represent the minimum and maximum magnitudes respectively, and σ is the rms error. The Amp is 73.67% for the B band and 79.96% for the R band. The Amp in the R band is larger than that in the B band. PMN J0948+0022 brightens by $\Delta R = 0^{\rm m}.66$ in about 6 days from MJD = 58885.71 to MJD = 58891.64, and fades by $\Delta R = 0^{\rm m}.65$ in about 4 days from MJD = 58909.6 to MJD = 58913.72, which is the fastest variability of this magnitude during our observation epochs. The magnitude changes are $\Delta R = 0^{\rm m}.59$ in about 7 days from MJD = 58933.56 to MJD = 58940.83 and $\Delta R = 0^{\rm m}.29$ in about 10 days from MJD = 59247.78 to MJD = 59257.73. The brightness increases by $\Delta R = 0^{\rm m}.64$ in 21 days from MJD = 58959.65 to MJD = 58980.67. Sub-flares are superimposed on the entire brightening trend. The magnitude variation in the B band is much smaller than that in the R band during the same time ($\Delta B = 0^{\rm m}.5$ from MJD = 58885.71 to MJD = 58891.64; $\Delta B = 0^{\rm m}.53$ from MJD = 58909.6 to MJD = 58913.72; $\Delta B = 0^{\rm m}.37$ from MJD = 58933.56 to MJD = 58940.83; $\Delta B = 0^{\rm m}.27$ from MJD = 59247.78 to MJD = 59257.73; $\Delta B = 0^{\rm m}.57$ from MJD = 58959.65 to MJD = 58980.67). The average magnitudes are $\langle m_{\rm R} \rangle = 17.72 \pm 0.01$ and $\langle m_{\rm B} \rangle = 17.88 \pm 0.01$.

3.2. Optical IDV

In order to search for optical IDV, F-test and one-way analysis of variance (ANOVA) are employed. The F-test and ANOVA are two different methods based on different principles to evaluate microvariability. The F-test is considered as a proper statistics to quantify optical IDV (e.g., de Diego 2010;

Table 2
Results of Optical IDV of PMN J0948+0022

Date (UT) (1)	Band (2)	N (3)	Time Spans (4)	F (5)	$F_C(99)$ (6)	F_A (7)	$F_A(99)$ (8)	V/N (9)	$\langle m\rangle$ (10)	$A(\%)$ (11)
2021-12-11	B	16	4.1	0.73	3.52	1.93	6.7	N	17.78	
2021-12-11	R	16	4.1	8.03	3.52	1.3	6.7	PV	17.67	3.9
2021-02-12	B	17	4.36	1.73	3.37	7.4	6.52	PV	17.75	6.7
2021-02-12	R	17	4.36	16.82	3.37	37.5	6.52	V	17.64	12.9
2020-12-20	B	15	4.68	1.32	3.7	0.043	6.93	N	17.94	
2020-12-20	R	15	3.84	6.36	3.7	1.45	6.93	PV	17.84	6.79
2020-12-19	B	17	5.05	3.31	3.37	1.5	6.52	N	17.95	
2020-12-19	R	17	5.05	4.6	3.37	3.97	6.52	PV	17.87	6.9
2020-05-15	B	11	1.38	1.41	4.85	1.81	10.56	N	17.8	
2020-05-15	R	11	1.38	19.28	4.85	2.95	10.56	PV	17.6	17.9
2020-05-11	B	21	2.82	2.72	2.93	12.08	5.18	PV	17.81	24.3
2020-05-11	R	21	2.82	19.81	2.93	11.77	5.18	V	17.6	29.9

Note. Columns 1–3 are the date of observations, the observed band and the number of data points, respectively. Column 4 is the time spans in units of hours. Column 5 is the average F value of F-test. Column 6 is the critical F value with a 99% confidence level. Column 7 is the F value of ANOVA. Column 8 is the critical F value of ANOVA with a 99% confidence level. Column 9 is variable status (V: variable; PV: probable variable; N: non-variable). Columns 10–11 are daily average magnitudes and variability amplitude in units of percent, respectively.

Joshi et al. 2011; Goyal et al. 2012; Hu et al. 2014; Xiong et al. 2016, 2017). It can be written as

$$F_1 = \frac{\mathrm{Var(Target\text{-}StarA)}}{\mathrm{Var(StarA\text{-}StarB)}},\ F_2 = \frac{\mathrm{Var(Target\text{-}StarB)}}{\mathrm{Var(StarA\text{-}StarB)}},$$
$$F = <F_1, F_2>, \tag{2}$$

where Var(target-StarA) and Var(target-StarB) stand for the variance of the differential instrumental magnitudes between target and comparison star, and Var(StarA-StarB) is the variance of the differential instrumental magnitudes between two comparison stars. The F value is calculated from the average of F_1 and F_2. If the F value is above the critical value $F^{\alpha}_{\nu_{\rm target},\nu_{\rm star}}$, the target is variable at the significance level α. $\nu_{\rm target}$ and $\nu_{\rm star}$ ($\nu = N - 1$) are the degrees of freedom for target and comparison star respectively, and α is set as 0.01 corresponding to a confidence level of 99%. The ANOVA is a powerful and robust estimator to search for optical IDV, because it does not rely on error measurement but derives the expected variance from sub-samples of the data (de Diego 2010; Xiong et al. 2017). The ANOVA classifies the data into inter-group and intra-group, and it compares the variances between the two groups. The detailed calculation formula can be found in Appendix A3 of de Diego (2010) and Equation (4) of Hong et al. (2017). If the F value of ANOVA is larger than the critical value $F^{\alpha}_{\nu_1,\nu_2}$, where $\nu_1 = k - 1$, $\nu_2 = N-k$ (k is the number of groups and N is the number of observation data), the target is variable at the significance level α. We bin the observation data in groups of five (and three) data points, and choose a confidence level of 99%.

The target is variable (V) when the light curves meet both of the variability criteria of F-test and ANOVA. The target is probably variable (PV) when the light curves meet one of the variability criteria of ANOVA and F-test. The target is not variable (N) when the light curves cannot meet any one of the variability criteria of ANOVA and F-test. We only analyze the night with the number of data points more than ten, so six nights are selected. The results of data analysis are given in Table 2. The V status is found in two nights (the R band on 2020 May 11 and 2021 February 12). The B band light curves on the two nights are detected as PV. The R band light curves in the rest of four nights are detected as PV. The light curves detected as PV and V status are shown in Figure 3. On 2020 May 11, the target fades by $\Delta R = 0\overset{\rm m}{.}14$ in 40.32 minutes from MJD = 58980.554 to MJD = 58980.582, and then brightens by $\Delta R = 0\overset{\rm m}{.}3$ in 120 minutes from MJD = 58980.582 to MJD = 58980.665, which correspond to Amp = 29.9%.

In order to quantify the reliability of variability, the differential instrumental magnitudes between two comparison stars (i.e., the instrumental magnitude of Ref A minus that of Ref B) are displayed in Figure 3. The differential instrumental magnitudes between two comparison stars are almost constant for the R band on 2020 May 11. For the B band on the same night, the trend of magnitude changes is consistent with that in the R band, but its Amp is much smaller compared to Amp in the R band. Although the light curve is considered as PV for the B band on 2020 May 11 (the ANOVA detects IDV but the F-test does not detect IDV), the F value of F-test is close to the critical value (see Table 2). On 2021 February 12, the R band light curve of PMN J0948+0022 continues to brighten by $\Delta R = 0\overset{\rm m}{.}13$ in 229 minutes from MJD = 59257.67 to MJD = 59257.83. For the B band on 2021 February 12, the ANOVA detects IDV but the F-test does not detect IDV. The daily average magnitudes on both 2020 May 11 and 2021 February 12 are above the average magnitudes during the whole monitoring epoch. For the R band light curves on 2021

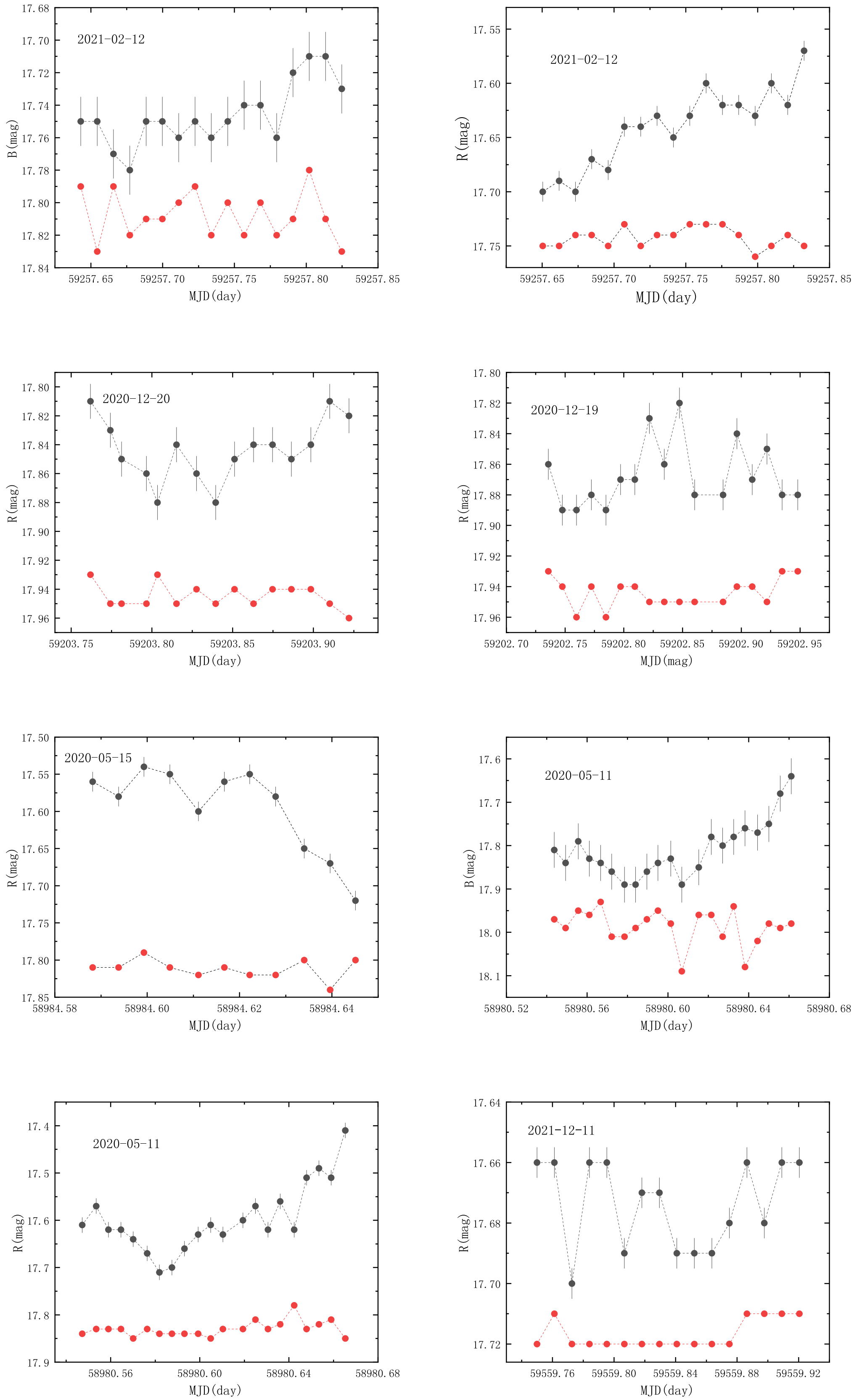

Figure 3. The light curves detected as PV and V status (same symbols as Figure 2).

December 11, 2020 December 20, 2020 December 19 and 2020 May 15, the F-test detects IDV but the ANOVA does not detect IDV.

The duty cycle (DC) of IDV is calculated by

$$\mathrm{DC} = 100\frac{\sum_{i=1}^{n} N_i (1/\Delta T_i)}{\sum_{i=1}^{n} 1/\Delta T_i}\%, \tag{3}$$

where $\Delta T_i = \Delta T_{i,\mathrm{obs}}(1+z)^{-1}$, z is the redshift and $\Delta T_{i,\mathrm{obs}}$ is the duration of the monitoring session of the ith night (Romero et al. 1999; Hu et al. 2014; Xiong et al. 2016). N_i will be set to 1 if IDV is detected, otherwise $N_i = 0$ (Goyal et al. 2013). For the R band, DC = 29% with Amp > 12.9%, and DC will be 100% with Amp > 3.9% when PV status is also considered. For the B band, only two nights are detected as PV status (2020 May 11 and 2021 February 12), DC = 0% for V status, and DC = 29% with Amp > 6.7% for PV status.

3.3. Correlation between Magnitude and Color Index

There are correlations between the $B-R$ index and R magnitude on intra-day and long timescales (see Figure 4). The spectral index is calculated as

$$\alpha_{\mathrm{BR}} = \frac{0.4(B-R)}{\log(\nu_{\mathrm{B}}/\nu_{\mathrm{R}})}, \tag{4}$$

where ν_{B} and ν_{R} are the effective frequencies of the respective bands (Wierzcholska et al. 2015). The average optical spectral index is $\langle \alpha_{\mathrm{BR}} \rangle = 0.32 \pm 0.01$ when considering all the observed data. The spectral index as y-axis is plotted in Figure 4. The error-weighted linear regression analyses show strong or moderate negative correlations between the $B-R$ index and R magnitude on intra-day timescale (see Table 3). For long timescale, a strong negative correlation between the $B-R$ index and R magnitude is found. Therefore, a redder-when-brighter (RWB) chromatic trend is significant for PMN J0948+0022 on intra-day and long timescales. When the R band magnitude is brighter than $17\overset{\mathrm{m}}{.}5$, color change trend disappears ($r = 0.17$, $P = 0.6$; the last panel in Figure 4).

3.4. Mass and Accretion Rate of SMBH

In light of the standard model of accretion disk (Shakura & Sunyaev 1973), the dimensionless accretion rate is defined as (Du et al. 2015)

$$\dot{\mathscr{M}} = 20.1\left(\frac{\ell_{44}}{\cos i}\right)^{3/2} M_7^{-2}, \tag{5}$$

where $\ell_{44} = L_{5100}/10^{44}\,\mathrm{erg\,s^{-1}}$ is the optical luminosity at rest wavelength 5100 Å, $M_7 = M_\bullet/10^7 M_\odot$ is the mass of SMBH and i is the inclination of accretion disk. We take $\cos i = 0.75$, which represents a mean disk inclination for type 1 AGNs. Therefore, we need to measure L_{5100} and estimate $M_\bullet$ before calculating the dimensionless accretion rate. Based on the single-epoch spectrum for PMN J0948+0022, $M_\bullet$ can be estimated using the virial equation

$$M_\bullet = f\frac{R_{\mathrm{H}\beta} v_{\mathrm{FWHM}}^2}{G}, \tag{6}$$

where $R_{\mathrm{H}\beta}$ is the radius of BLR for broad emission line Hβ, v_{FWHM} is the velocity FWHM of broad Hβ, G is the gravitational constant, and f is the virial factor which is usually taken as $f = 1.0$ for v_{FWHM}.

The spectral fitting scheme is widely used in spectral analysis (e.g., Hu et al. 2015; Lu et al. 2019), which can eliminate the contamination of other blended components in our measurement. Following the work of Lu et al. (2021a), we decomposed the spectrum into multi-components in the Hγ and Hβ region (see Figure 5). The main fitting models include power law for AGN continuum (blue), Fe II template for strong iron lines (green), two Gaussians for the broad Hβ (pink), two Gaussians for the broad Hγ (pink), and one Gaussian for the broad He II line (cyan). From the decomposed spectrum, we measured the continuum flux density at 5100 Å $F_{5100,\mathrm{disk+jet}} = 9.39 \times 10^{-17}\,\mathrm{erg\,s^{-1}\,cm^{-2}\,Å^{-1}}$ and $v_{\mathrm{FWHM}} = 1659\,\mathrm{km\,s^{-1}}$ for the broad Hβ, and calculated the flux ratio of Fe II to Hβ $R_{\mathrm{Fe}} = 1.26$. The RWB trend of PMN J0948+0022 appears/disappears when the magnitude is fainter/brighter than $R = 17\overset{\mathrm{m}}{.}5$ (more details see Section 4), which indicates that the optical contributions from thermal radiation of accretion disk and non-thermal radiation of jet reach an equilibrium when $R = 17\overset{\mathrm{m}}{.}5$, that is, the continuum flux density from the accretion disk $F_{5100,\mathrm{disk}}$ should be half of $F_{5100,\mathrm{disk+jet}}$. Therefore, we calculated $F_{5100,\mathrm{disk}} = 5.85 \times 10^{-17}\,\mathrm{erg\,s^{-1}\,cm^{-2}\,Å^{-1}}$ by the difference between $R = 17\overset{\mathrm{m}}{.}5$ and $17\overset{\mathrm{m}}{.}74$ ($R = 17\overset{\mathrm{m}}{.}74$ during the spectroscopic observation, see Section 2.2). The optical luminosity L_{5100} is derived from $F_{5100,\mathrm{disk}}$ with the cosmological parameters of $H_0 = 72\,\mathrm{km\,s^{-1}\,Mpc^{-1}}$, $\Omega_\Lambda = 0.7$, and $\Omega_{\mathrm{M}} = 0.3$. Therefore, using the latest scaling relation of Du & Wang (2019), we estimated $M_\bullet = 1.61 \times 10^7 M_\odot$ for PMN J0948+0022. With L_{5100} and $M_\bullet$, we obtained $\dot{\mathscr{M}} = 93$. According to the classification of sub-Eddington and super-Eddington ($\dot{\mathscr{M}} \geqslant 3$) of Du et al. (2015), we found that PMN J0948+0022 is a super-Eddington accreting AGN.

4. Discussion

For nearby AGNs, when performing aperture photometry, the contribution from a strong host galaxy component has a significant impact on the photometry results (Cellone et al. 2000; Nilsson et al. 2007). If there is a large seeing change, false microvariability is likely to occur. PMN J0948+0022 has no clear features of host galaxy, and its host galaxy is much fainter than its AGN core (Liu et al. 2010). Moreover, the photometric aperture was always greater than 2 × FWHM, so the host galaxy was included in the aperture even if the target had a host galaxy. An aperture radius of 2 × FWHM is expected to yield fairly reliable light curves for the AGN even

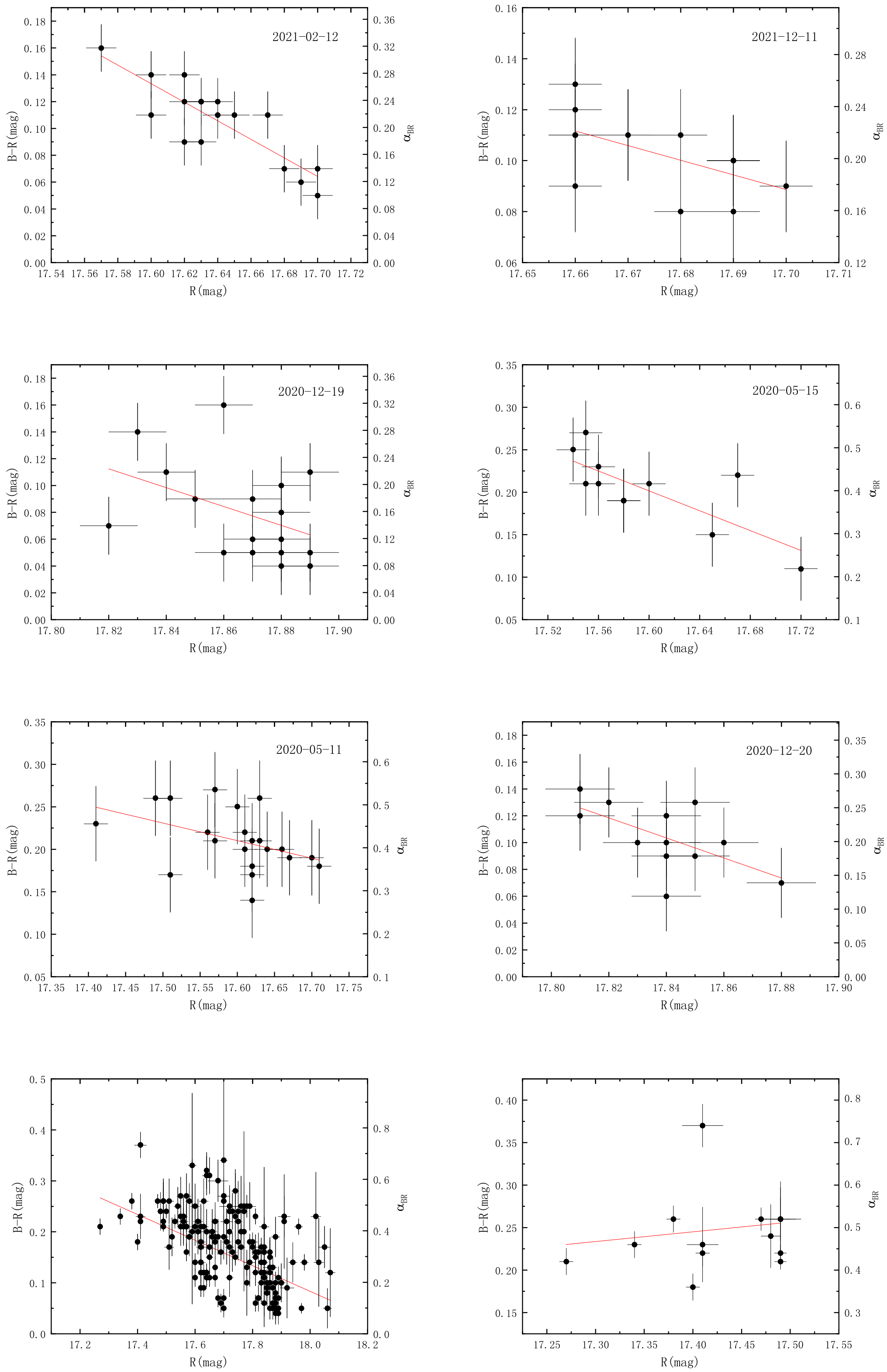

Figure 4. Correlations between the $B-R$ index (spectral index $\alpha_{\rm BR}$) and R magnitude. The y-axis on the left represents the $B-R$ index and the right represents spectral index $\alpha_{\rm BR}$. The left panel in the last row represents the data of for the whole monitoring epoch. The right panel in the last row is for the data when considering brightness more than $17\overset{\rm m}{.}5$. The red lines are the results of error-weighted linear regression analysis.

Table 3
Results of Error-weighted Linear Regression Analysis

Date (UT)	r	P
2021-02-12	−0.85	$<10^{-4}$
2021-12-11	−0.62	0.01
2020-12-19	−0.42	0.09
2020-05-15	−0.77	6×10^{-3}
2020-05-11	−0.43	0.05
2020-12-20	−0.61	0.03
All data	−0.5	$<10^{-4}$

Note. r is the coefficient of correlation and P is the chance probability.

if its host galaxy is up to 2 mag brighter (Cellone et al. 2000; Ojha et al. 2020). Therefore, the host galaxy cannot significantly take effects on our photometry results, i.e., the contamination of the host galaxy is negligible.

There is IDV in two nights for the R band and possible IDV in all the six nights. DC = 29% with Amp > 12.9% in the R band. In fact, the target had a higher IDV duty cycle (DC > 50%) (Liu et al. 2010; Paliya et al. 2013; Ojha et al. 2020, 2021). For the B band light curves, the possible IDV was detected only in the two nights. The following three factors are likely to make a lower DC value for our results: short time spans per night (<4 hr), a larger scatter in the differential instrumental magnitudes between two comparison stars, and lack of enough data points. Previous studies demonstrated a longer duration per night and a higher possibility of IDV detection (Gupta & Joshi 2005; Rani et al. 2011). The larger scatter may cause a lower F value of F-test. The lack of enough data points may reduce the possibility of detecting IDV. It's also possible that during our monitoring epochs the target indeed has a lower DC value compared to other epochs. Goyal et al. (2013) found DC ≈ 32% with Amp > 3% for TeV γ-ray blazars. If higher Amp is considered, DC should be lower for TeV γ-ray blazars. Thus, DC = 29% with Amp > 12.9% in our results is comparable to that of TeV γ-ray blazars. These comparable DC values support a similar IDV nature and the presence of relativistic jets with a small angle of view in the γ-ray emitting NLS1 galaxies. High IDV is often considered to be an important feature for blazars, and is related to the relativistic jets with a small angle of view (e.g., Wagner & Witzel 1995; Sagar et al. 2004; Goyal et al. 2013). We found the high IDV on 2020 May 11 when the target brightened by $\Delta R = 0\overset{\mathrm{m}}{.}3$ in 120 minutes, corresponding to Amp = 29.9%. The average magnitude on the night is above that during the whole monitoring epoch. Such high IDV also supports a similar IDV nature between γ-ray emitting NLS1 galaxies and blazars, and the presence of relativistic jets with a small angle of view. For long timescale, the object displays significant variability in the B and R bands, which is similar to variability of blazars.

Amp = 73.67% for the B band and Amp = 79.96% for the R band when considering all the observed data. For many obvious flares, $|\Delta B|$ is much smaller than $|\Delta R|$ (see Section 3.1). Amp in the R band is larger than that in the B band for the two nights detected as IDV (see Table 2), i.e., variability in higher frequencies exhibits lower amplitude. Our results show that an RWB chromatic trend is significant for PMN J0948+0022 on intra-day and long timescales. The shock-in-jet model is often used to explain the variability and bluer-when-brighter (BWB) trend in blazars (e.g., Marscher & Gear 1985; Xiong et al. 2017; Liu et al. 2019; Feng et al. 2020a, 2020b). Disturbances in the flow of a jet cause a shock to propagate along the jet. When the shock sweeps emitting regions, variability/flare occurs. Higher frequency photons from the synchrotron mechanism typically emerge sooner and closer to the shock front than lower frequency radiation, resulting in higher variability amplitude of higher frequency photons and a BWB trend (Agarwal & Gupta 2015). However, the shock-in-jet model is hard to explain our results, i.e., an RWB trend.

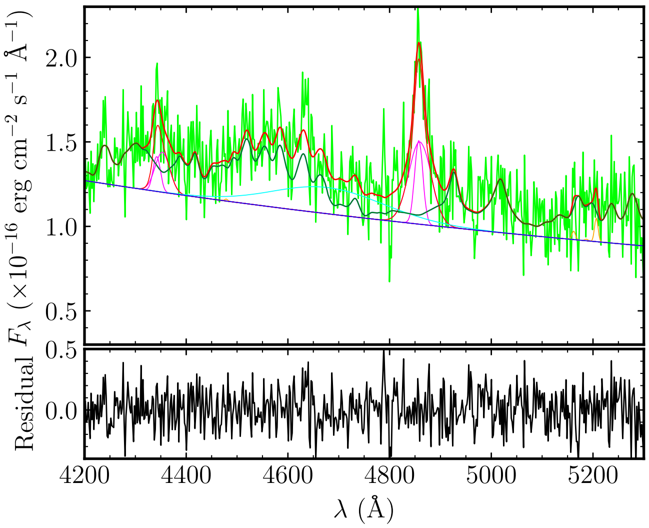

Figure 5. Fitting and multi-component decomposition of the spectrum observed from the Lijiang 2.4 m telescope (JD = 2459622). The top panel shows the details of spectral fitting and decomposition and the bottom panel shows the residuals.

The BWB chromatic trend is significant in most blazars, especially BL Lac objects (e.g., Feng et al. 2020a, 2020b), whereas the RWB trend is also found for flat-spectrum radio quasars (FSRQs) (e.g., Gu et al. 2006; Wu et al. 2007; Ikejiri et al. 2011; Bonning et al. 2012; Dai et al. 2015; Xiong et al. 2020). The different relative contributions of the thermal versus non-thermal radiation to the optical emission may be responsible for the different trends of the color index with brightness in FSRQs and BL Lac objects (Gu et al. 2006). The color change trend may be dominated by the relative position changes of the synchrotron peak frequency of spectral energy distribution (SED) with respect to the observational window (e.g., Feng et al. 2020a, 2020b). So, the color change trend may be controlled by the observational window and the underlying broadband SED. The broadband SED fitting shows that accretion disk dominates the total optical flux in a lower state, and our observational window is to the left of the peak of accretion disk SED and to the right of the peak of synchrotron SED of jet (see Figure 4 in Abdo et al. 2009a). A BWB trend emerges for radiation of accretion disk and jet as they brighten, and furthermore our observational window is to the left of the peak of accretion disk SED and to the right of the peak of synchrotron SED of jet as PMN J0948+0022 is between the lowest and highest states (see Figure 6 in Foschini et al. 2015). From lower to higher state, a superposition of the BWB trends of the jet and disk components will lead to an RWB trend because that the jet component is much redder than the disk one and that the jet component contributes more relative to the disk one. The BWB trend in disk emission of PMN J0948+0022 is consistent with the results that the thermal component of accretion disk dominates the total emission in low flux state and that accretion disk model can produce the BWB trend (Li & Cao 2008; Gu & Li 2013; Xiong et al. 2020). When PMN J0948+0022 is in the highest state, the total SED seems to be flat in our observational window (nearly equal jet and disk contributions), and the color change trend likely becomes saturated (see Figure 6 in Foschini et al. 2015). This saturation is consistent with the result of Isler et al. (2017) that the color change trend remains unchanged when jet and disk contributions are equal. Also, this saturation is consistent with the disappearance of the color change trend in PMN J0948+0022 when brighter than $17^{\mathrm{m}}.5$ in the R band.

The jet component on short timescale might be more variable compared to the accretion disk component due to the jet beaming effect. The accretion disk component seems more variable on long timescale. Liu et al. (2010) found that PMN J0948+0022 emerges $\Delta R = 0^{\mathrm{m}}.5$ within a few hours when the brightness is higher than $17^{\mathrm{m}}.33$. Our results show that the target brightened by $\Delta R = 0^{\mathrm{m}}.3$ in 120 minutes when the brightness is lower than $17^{\mathrm{m}}.4$. Therefore, the target shows higher variability amplitude when brighter. With respect to the optical emission of accretion disk, the jet in PMN J0948+0022 may be weak on long timescale. Interestingly, PMN J0948+0022 is a super-Eddington accreting NLS1 galaxy with the highest redshift among those known super-Eddington accreting NLS1s, some of which were used as candidates of cosmological candle (e.g., Wang et al. 2014). PMN J0948+0022 expands the redshifts of those NLS1s by almost an order of magnitude up to above 0.5, and increasing largely the cosmological distance of target is important to use super-Eddington accreting NLS1s as candidates of cosmological candle. PMN J0948+0022 may be used as a target for the next step of reverberation mapping monitoring project of SEAMBHs.

5. Conclusions

We have monitored the γ-ray emitting NLS1 galaxy PMN J0948+0022 in the B and R bands from 2020 to 2021. We have also performed the spectral observation on 2022 February 11. Our main conclusions are as follows.

(i) The RWB chromatic trend in PMN J0948+0022 is dominant on intra-day and long timescales, resembles those in FSRQs, and is dominated by the accretion disk and jet radiation. When considering the data brighter than $R = 17^{\mathrm{m}}.5$, no color change trend appears. The optical IDV was detected in two nights. Our results of variability indicate the presence of relativistic jets with a small angle of view, which is similar to blazars.

(ii) Based on spectral observation, we get $M_{\bullet} = 1.61 \times 10^7 M_{\odot}$ and $\dot{\mathscr{M}} = 93$ for the SMBH in PMN J0948+0022, and identify that PMN J0948+0022 is a super-Eddington accreting AGN. PMN J0948+0022 expands the redshifts of those known super-Eddington accreting NLS1s by almost an order of magnitude up to above 0.5. Some of those NLS1s were adopted as candidates of cosmological candle. It may be used as a target for the next step of reverberation mapping monitoring project of SEAMBHs.

(iii) The magnitude fades by $\Delta R = 0^{\mathrm{m}}.65$ in about 4 days, which is the shortest timescale of variations with such a large magnitude change ($\Delta R > 0^{\mathrm{m}}.5$) during our observation epochs. When considering all the observed data, the average magnitudes are $\langle m_{\mathrm{R}} \rangle = 17.72 \pm 0.01$ and $\langle m_{\mathrm{B}} \rangle = 17.88 \pm 0.01$, and the average optical spectral index is $\langle \alpha_{\mathrm{BR}} \rangle = 0.32 \pm 0.01$.

(iv) On 2020 May 11, the target fades by $\Delta R = 0^{\mathrm{m}}.14$ in 40.32 minutes and then brightens by $\Delta R = 0^{\mathrm{m}}.3$ in 120 minutes corresponding to Amp = 29.9%. The DC value is 29% with Amp > 12.9% in the R band. On long timescale, the object displays significant variability in the B and R bands.

(v) The variability amplitude is 73.67% for the B band and 79.96% for the R band when considering all the observed data. For many obvious flares, the amplitude of magnitude changes in the B band is much smaller than that in the R band. The Amp in the R band is larger than that in the B band for the two nights detected as IDV, i.e., variability in higher frequencies detects lower amplitude.

Acknowledgments

We are very grateful to the anonymous referee for constructive comments leading to significant improvement of this paper. We think very much to Yang Huang for his help with photometric data reduction. This work is supported by the National Key R&D Program of China with No. 2021YFA1600404, the National Natural Science Foundation of China (NSFC, grant Nos. 11991051, Y911080201, 12073068, 11673062, 11703077, 11703078), the CAS "Light of West China" Program, the Yunnan Province Foundation (2019FB004, 202001AT070069), Yunnan Province Youth Top

Talent Project (YNWR-QNBJ-2020-116), and the science research grants from the China Manned Space Project with NO. CMS-CSST-2021-A06 and CMS-CSST2021-A05. This research has made use of NASA's Astrophysics Data System Bibliographic Services and the NASA/IPAC Extragalactic Database (NED), which is operated by the Jet Propulsion Laboratory, California Institute of Technology, under contract with the National Aeronautics and Space Administration. We acknowledge the use of the Lijiang 2.4 m telescope and its technical operation and maintenance team. This research uses data obtained through the Lijiang 2.4 m Telescope, which is funded by the Chinese Academy of Sciences, the People's Government of Yunnan Province and the National Natural Science Foundation of China.

ORCID iDs

Yu-Xin Xin https://orcid.org/0000-0003-1991-776X
Kai-Xing Lu https://orcid.org/0000-0002-2310-0982

References

Abdo, A. A., Ackermann, M., Ajello, M., et al. 2009a, ApJ, 699, 976
Abdo, A. A., Ackermann, M., Ajello, M., et al. 2009c, ApJ, 707, 727
Abdo, A. A., Ackermann, M., Ajello, M., et al. 2009b, ApJ, 707, 142
Agarwal, A., & Gupta, A. C. 2015, MNRAS, 450, 541
Ajello, M., Angioni, R., Axelsson, M., et al. 2020, ApJ, 892, 105
Baldi, R. D., Capetti, A., Robinson, A., Laor, A., & Behar, E. 2016, MNRAS: Lett., 458, L69
Bertin, E., & Arnouts, S. 1996, A&AS, 117, 393
Berton, M., Foschini, L., Ciroi, S., et al. 2015, A&A, 578, 28
Boller, T., Brandt, W. N., & Fink, H. 1996, A&A, 305, 53
Bonning, E., Urry, C. M., Bailyn, C., et al. 2012, ApJ, 756, 13
Calderone, G., Ghisellini, G., Colpi, M., & Dotti, M. 2013, MNRAS, 431, 210
Cellone, S. A., Romero, G. E., & Combi, J. A. 2000, AJ, 119, 1534
Dai, B.-Z., Zeng, W., Jiang, Z.-J., et al. 2015, ApJS, 218, 18
D'Ammando, F. 2020, MNRAS, 498, 859
de Diego, J. A. 2010, AJ, 139, 1269
Du, P., Hu, C., Lu, K.-X., et al. 2014, ApJ, 782, 45
Du, P., Hu, C., Lu, K.-X., et al. 2015, ApJ, 806, 22
Du, P., & Wang, J.-M. 2019, ApJ, 886, 42
Eggen, J. R., Miller, H. R., & Maune, J. D. 2013, ApJ, 773, 85
Fan, J. H., Kurtanidze, O., Liu, Y., et al. 2014, ApJS, 213, 26
Fan, Y.-F., Bai, J.-M., Zhang, J.-J., et al. 2015, RAA, 15, 918
Feng, H.-C., Liu, H.-T., Bai, J.-M., et al. 2020a, ApJ, 888, 30
Feng, H.-C., Yang, S., Yang, Z.-X., et al. 2020b, ApJ, 902, 42
Foschini, L., Ghisellini, G., Kovalev, Y. Y., et al. 2011, MNRAS, 413, 1671
Foschini, L., Berton, M., Caccianiga, A., et al. 2015, A&A, 575, A13
Goodrich, R. W. 1989, ApJ, 342, 224
Goyal, A., Gopal-Krishna, G. K., Wiita, P. J., Stalin, C. S., & Sagar, R. 2013, MNRAS, 435, 1300
Goyal, A., Gopal-Krishna, G. K., Wiita, P. J., et al. 2012, A&A, 544, A37
Gu, M. F., & Ai, Y. L. 2011, A&A, 534, A59
Gu, M., Chen, Y., Komossa, S., et al. 2015, ApJS, 221, 3
Gu, M. F., Lee, C. U., Pak, S., Yim, H. S., & Fletcher, A. B. 2006, A&A, 450, 39
Gu, M. F., & Li, S. L. 2013, A&A, 554, A51
Gupta, A. C., & Joshi, U. C. 2005, A&A, 440, 855
Heidt, J., & Wagner, S. J. 1996, A&A, 305, 42
Hong, S., Xiong, D., & Bai, J. 2017, AJ, 154, 42
Howell, S. B. 2006, Handbook of CCD Astronomy (2nd ed.; Cambridge: Cambridge Univ. Press)
Hu, C., Du, P., Lu, K.-X., et al. 2015, ApJ, 804, 138
Hu, S.-M., Chen, X., Guo, D. F., Jiang, Y. G., & Li, K. 2014, MNRAS, 443, 2940
Ikejiri, Y., Uemura, M., Sasada, M., et al. 2011, PASJ, 63, 639
Isler, J. C., Urry, C. M., Coppi, P., et al. 2017, ApJ, 844, 107
Itoh, R., Tanaka, Y. T., Fukazawa, Y., et al. 2013, ApJL, 775, L26
Joshi, R., Chand, H., Gupta, A. C., & Wiita, P. J. 2011, MNRAS, 412, 2717
Kellermann, K. I., Condon, J. J., Kimball, A. E., Perley, R. A., & Ivezić, Ž. 2016, ApJ, 831, 168
Komossa, S., Voges, W., Xu, D., et al. 2006, AJ, 132, 531
Kron, R. G. 1980, ApJS, 43, 305
Kshama, S. K., Paliya, V. S., & Stalin, C. S. 2017, MNRAS, 466, 2679
Li, S. L., & Cao, X. 2008, MNRAS: Lett., 387, L41
Liu, H.-T., Feng, H.-C., Xin, Y.-X., et al. 2019, ApJ, 880, 155
Liu, H., Wang, J., Mao, Y., & Wei, J. 2010, ApJL, 715, 113
Lu, K.-X., Wang, J.-G., Zhang, Z.-X., et al. 2021a, RAA, 21, 183
Lu, K.-X., Wang, J.-G., Zhang, Z.-X., et al. 2021b, ApJ, 918, 50
Lu, K.-X., Zhao, Y.-H., Bai, J.-M., & Fan, X.-L. 2019, MNRAS, 483, 1722
Marscher, A. P., & Gear, W. K. 1985, ApJ, 298, 114
Maune, J. D., Miller, H. R., & Eggen, J. R. 2013, ApJ, 762, 124
Nilsson, K., Pasanen, M., Takalo, L. O., et al. 2007, A&A, 475, 199
Ojha, V., Chand, H., & Gopal-Krishna, G. K. 2021, MNRAS, 501, 4110
Ojha, V., Chand, H., Krishna, G., Mishra, S., & Chand, K. 2020, MNRAS, 493, 3642
Osterbrock, D. E., & Pogge, R. W. 1985, ApJ, 297, 166
Paliya, V. S., Stalin, C. S., Kumar, B., et al. 2013, MNRAS, 428, 2450
Pogge, R. W. 2000, NewAR, 44, 381
Rani, B., Gupta, A. C., Joshi, U. C., Ganesh, S., & Wiita, P. J. 2011, MNRAS, 413, 2157
Romero, G. E., Cellone, S. A., & Combi, J. A. 1999, A&AS, 135, 477
Sagar, R., Stalin, C., Gopal-Krishna, G. K., & Paul, J. 2004, MNRAS, 348, 176
Schlafly, E. F., & Finkbeiner, D. P. 2011, ApJ, 737, 103
Schlegel, D. J., Finkbeiner, D. P., & Davis, M. 1998, ApJ, 500, 525
Shakura, N., & Sunyaev, R. 1973, A&A, 24, 337
Shuder, J. M., & Osterbrock, D. E. 1981, ApJ, 250, 55
Urry, C. M., & Padovani, P. 1995, PASP, 107, 803
Wagner, S. J., & Witzel, A. 1995, ARA&A, 33, 163
Wang, C.-J., Bai, J.-M., Fan, Y.-F., et al. 2019, RAA, 19, 149
Wang, F., Xiong, D.-R., Bai, J.-M., Li, S.-K., & Wang, J.-G. 2017, RAA, 17, 68
Wang, J.-M., Du, P., Valls-Gabaud, D., Hu, C., & Netzer, H. 2013, PhRvL, 110, 081301
Wang, J.-M., Du, P., Hu, C., et al. 2014, ApJ, 793, 108
Wierzcholska, A., Ostrowski, M., Stawarz, A., Wagner, S., & Hauser, M. 2015, A&A, 573, A69
Williams, R. J., Richard, W., & Smita, M. 2002, AJ, 124, 3042
Wu, J., Zhou, X., Ma, J., et al. 2007, AJ, 133, 1599
Xiong, D.-R., Bai, J.-M., Zhang, H.-J., et al. 2017, ApJS, 229, 21
Xiong, D.-R., Zhang, H.-J., Zhang, X., et al. 2016, ApJS, 222, 24
Xiong, D., Bai, J., Fan, J., et al. 2020, ApJS, 247, 49
Yao, S., Komossa, S., Liu, W. J., et al. 2019, MNRAS: Lett., 487, L40
Yuan, W., Zhou, H. Y., Komossa, S., et al. 2008, ApJ, 685, 801
Zhang, X., Zheng, Y. G., Zhang, H. J., & Hu, S. M. 2008, ApJS, 174, 111
Zhou, H.-Y., Wang, T.-G., Dong, X.-B., Zhou, Y.-Y., & Li, C. 2003, ApJ, 584, 147
Zhou, H.-Y., Wang, T.-G., Yuan, W.-M., et al. 2006, ApJS, 166, 128